The Scanning Tunneling Atom Probe, and Lensless Point Reflection Microscopy

J.C.H. Spence

Physics and Astronomy, Arizona State University,
Tempe, AZ 85287, USA.
email spence@asu.edu

(Received: Jan. 30, 1997 Accepted: Feb. 19, 1997)

Abstract

In this paper we summarise the development of two new scientific instruments intended to assist the nanostructural characterisation of new materials. Firstly, our Scanning Tunneling Atom Probe (STAP) is described. This is a conventional Scanning Tunneling Microscope (STM) which allows atom clusters of interest on clean surfaces to be picked up and transferred into a time-of-flight spectrometer for atomic number identification. The second instrument, the Point Reflection Microscope (PRM) addresses the need for a "table-top" lensless electron microscope for imaging clean crystal surfaces in ultra-high vacuum.

1. The Scanning Tunnelling Atom Probe (STAP)

In recent work on the formation and study of man-made structures at the nanoscale level[1], one crucial piece of evidence is often missing - the chemical identification of the atomic species at identified crystallographic sites. Thus there is an urgent need for a technique which is capable of identifying atoms observed, for example, in STM[2] or TEM images. Impurities often control the properties of materials, yet these cannot be identified on extended surfaces by any atomic resolution microscopy, despite the power of the atom probe for samples which can be formed into tips for controlled field-evaporation. The STAP instrument we have developed[3] may make this possible. Applications of such an instrument would then include the measurement of diffusion profiles at interfaces (quantum wells, grain boundaries, ceramic-metal), the study of non-stoichiometry during crystal growth, the identification of foreign species at special sites, such as kinks and steps, during crystal growth and the study of their effect on growth kinetics. Segregation at defects such as the Cotrell atmospheres which form around emerging dislocation cores could also be studied, as could the atomic mechanisms involved in surfactant motion during crystal growth. The possibility of picking up fragments of large molecules lying on surfaces for analysis also arises (in correlation with their atomic resolution images). Other possibilities include continuous erosion for three-dimensional compositional analysis, research into catalyst poisoning, and the study of changes in surface composition due to surface diffusion at elevated temperatures.

Previous methods for chemical analysis at the nanoscale include the atom probe, transmission energy loss spectroscopy (ELS) and scanning auger microscopy (SAM). Both the latter use the subnanometer probe of a transmission electron microscope: the first is capable of identifying a few atoms within a thin film from their ELS spectra (in correlation with an atomic resolution image of the projected structure)[4], the second has very recently achieved a resolution of about 2 nm for surface imaging of bulk samples[5].

Figure 1 shows the general arrangement of our new STAP instrument. It is housed in a UHV chamber. By applying a short voltage pulse to the tip at a region of interest in an STM image, atoms are transferred from this region onto the tip. The sample is then removed, and a much larger voltage pulse applied, causing field evaporation of these atoms into a time-of-flight spectrometer for mass identification, as in the atom probe[6]. Instruments related to ours, but intended for different purposes, have been described by Nishikawa and Sakurai amongst others[7]. Our instrument arose from previous work studying material transferred between a tip and a sample using an STM operating within a TEM. The TEM was operated in the reflection mode during STM tunneling[8].

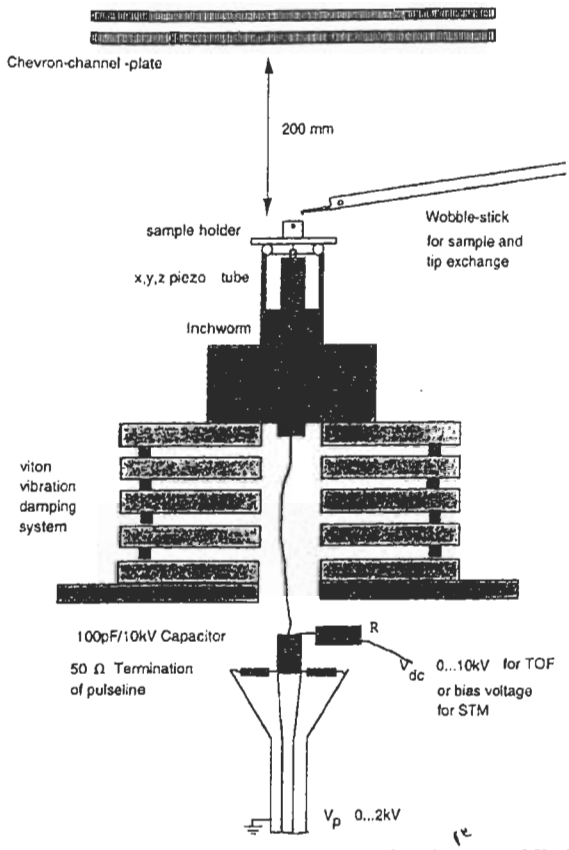

Fig. 1 General arrangement of the STAP instrument, not to scale.

A tube scanner is used to support the sample holder, which sits on three balls, and may be removed to a heating station. The scanner provides all fine motion in X,Y and Z. Tunnel current is obtained from the sample via a conducting support ball connected to the input of a current preamplifier. The non-scanning tip is fixed to the end of a Burleigh inchworm which is used for z-motion. This arrangement simplifies high voltage (<15kV) connections to the tip for field-evaporation. The inner scan tube electrode supports up to 15 kV electrical isolation from the tip. The tip sits in a removable kinematic mount, allowing it to be removed for cleaning by heating, field evaporation or sputtering. The bias lead to the tip passes to a ceramic UHV high voltage capacitor (which supplies the field evaporation pulse, < 2 kV), through a 5 kOhm UHV resistor to a vacuum feedthrough, to which either the bias (STM mode) or the <10 kV d.c. field evaporation voltage is supplied. The resistor prevents pulse reflections from the DC supply and does not interfere with STM operation. The 50 ohm pulse line supplies a < 2kV, 10 ns wide pulse to the tip. Ions are detected in TOF mode by a two-stage chevron channel plate, capable of single ion detection. A biased fluorescent screen allows observation of either the electron field emission image from the tip or the field ion image of the tip. Capacitive coupling to the screen leads the ion signal to a digital oscilloscope, which is triggered by the 10 ns pulse to the tip. The scope transfers spectra to a small computer using Labview software, which initiates pulsing, provides a graphic user interface, and accumulates a histogram of ion flight times, labelled with m/n values. A leak valve provides a supply of neon imaging gas, which may also be used for sputter sharpening the tip. This form of atom probe resembles the imaging atom probe design of Panitz[9].

For a total effective potential V_{eff} at the tip, the mass to charge ratio m/n is obtained from the energy conservation equation $n e V_{eff} = (1/2) m v^2 = (1/2) m (L/t)^2$, where t is the flight time, m the atomic mass, n the ionic charge and L = 200mm (figure 1). Ion trajectories in electrostatic fields are independent of m/n. The effective potential is calibrated using spectra from tungsten tips containing both W^{3+} and W^{4+} peaks. The mass resolution of the TOF spectrometer is influenced by several factors including the variation in time between axial and marginal rays (2% error) and the shape of the evaporation pulse (ions leaving the tip at the beginning of the pulse are accelerated for longer than those emitted near the end). We expect about $\Delta m/m = 2\Delta t/t = 1/50$ (i.e. 2%) due to the variation in flight time alone - the resolution we measure (about 4%) may be due to additional energy deficit effects from the tip pulse shape. (The Si^{28} isotope accounts for 92% abundance, so that an isotopic energy spread is not expected). The choice of L is a compromise between improved mass resolution (larger L) and the need to enlarge the angular view of the tip (about 20° full width in this design). This limits the size of the region on the tip from which atoms can reach the detector.

Figure 2 shows the Si (111) 7×7 structure we have used to test the instrument. The doped sample was resistively heated to 1350°C and cooled through the phase transition at 830°C. The figure shows the effects of a 5 volt , 20 ms pulse applied to the sample (tip positive). After pulsing, the right hand image was obtained in a second scan (with the transferred material still on the tip). The images are identical except for the pit where a cluster of atoms have been transferred to the tip. A time of flight spectrum from this region is shown in figure 3 - a later

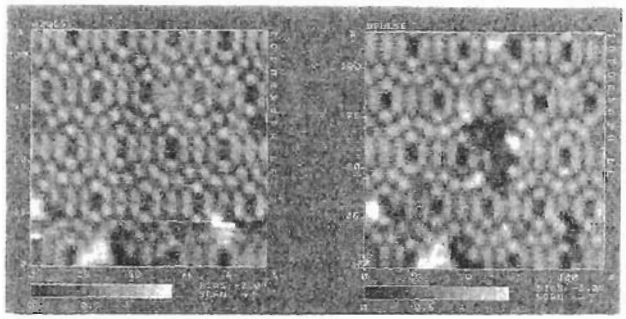

Fig. 2 Identical Si 7×7 regions before (left) and after (tight) applying a 10 msec positive 5 volt pulse to the tip near the center of the image, showing modification to the surface.

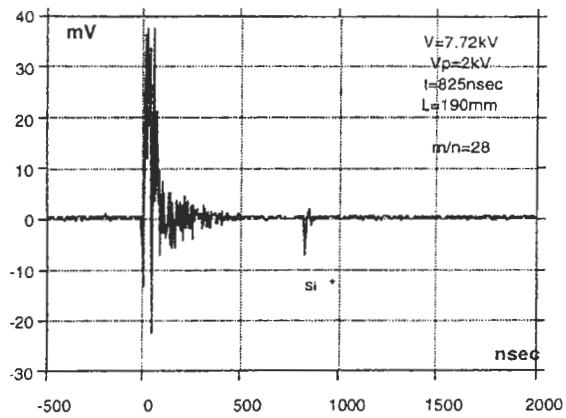

Fig. 3 Time of flight spectrum showing the Si^{++} peak from a cluster of atoms trasferred from the surface of a silicon crystal. A spectrum showing the Si^{++} peak was also obtained. Oscillations near time origin are radio frequency noise, since suppressed by improved shielding.

pulse also produced the Si^{++} peak. Further experiments have confirmed that STM scanning with a clean tip does not produce Si peaks in the spectrum without low voltage pulsing for transfer of material.

These are preliminary results. So far, we have not succeeded in finding the same region of sample for STM imaging after performing spectroscopy. However one sample holder includes a straight, vee-shaped groove, into which two of the three supporting balls fit. This constrains the stage motion to one dimensional motion. Since the stage can easily be positioned to within 100 microns (0.1mm) along this track using the wobble-stick, and since the lateral range of the scan tube is 4 microns, only 25 frames need be searched to find the same area again.

A considerable literature exists on experiments and theory for atom transfer and manipulation by STM[10,11]. Two regimes have been distinguised - large and small gaps. For microanalysis we require atomic transport from sample to tip only. For small gaps, this depends on tip polarity and the relative field evaporation thresholds E_v for the tip and sample. For small gaps with W tips on Si where chemical forces act, a negative tip produces most efficient transfer. There is evidence that, for large gaps (>1nm) material flows from sample to tip independent of polarity, since ions of both types may form in response to the fieldl[2]. In general, refractory metal tips should be used for microanalysis of softer materials. For silicon and tungsten, $E_v(W) = E_v(Si) + 2$ eV. For large tunneling gaps, some field enhanced diffusion of adsorbed species may occur[3], degrading spatial resolution. This effect will depend on the pulse length, temperature, gap size and diffusion coefficients. In the time-gated mode, an elemental map of the distribution of sample atoms adsorbed on the tip might be obtained[14]. A comparison of these images with the STM pit images may be instructive. Due to the limited open area of the channel-plate, ion detection is known to be less than 100% efficient. We therefore do not expect that this method will always be capable of single-atom detection, and the statistical sensitivity remains to be evaluated. An atomic force microscope (AFM) variant of the instrument is under consideration. Experiments with Ge deposits on Si are under way in order to determine the smallest number of atoms which can be identified. At present, with no tip cooling, the instrument is limited to species which do not diffuse appreciably at room temperature -cooling facilites would be needed to study metal adatoms, for example.

2. The Point Reflection Microscope

Figure 4 shows the principle of the point reflection microscope (PRM) we have developed[15] in simplified form. A nanotip electron field-emitter S at about 100 - 1000 volts is placed a distance z_1 above an atomically flat crystalline substrate. This acts as a mirror, a sample, and a grounded anode. The specular reflected divergent beam then appears to come from a virtual source S' below the surface. If the surface were a perfect mirror the arrangement would be equivalent to point-projection imaging from below the sample in the transmission geometry , so that shadow images of small opaque objects lying on the

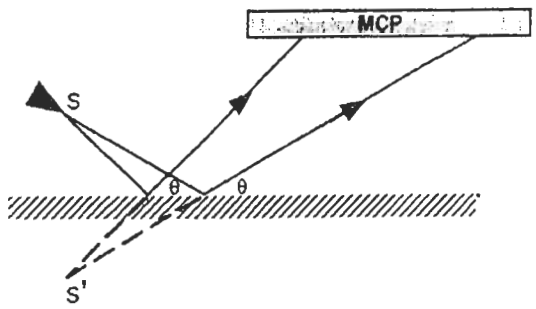

Fig. 4 Principle of the point-reflection electron microscope, showing shadow image formation by mirror reflection. The image is projected from the virtual source S'.See also figure 10.

mirror surface would be seen on the microchannel plate (MCP) detector screen, with magnification $M = (z_2+z_1)z_1$. Here z_2 is the distance from sample to detector, about 14 cm in our instrument. Since the beam is highly coherent, surface steps will be revealed by Fresnel fringes due to the "focus defect" z_1 as in the low voltage, lensless point-projection microscope[16-19].

GaAs crystals, cleaved in vacuo on (100) were used as samples, in view of their excellent cleavage properties and high conductivity, and because of the high quality reflection images which have been produced from them previously in TEM instruments[20]. Since most of the electrostatic potential is dropped very close to a sharp tip[21] , trajectories are reasonably straight if the sample is in the far-field of the tip. The direction of the beam is then fixed mainly by the asperity on the tip rather than by the sample orientation, and the electrons gain most of their kinetic energy within a few hundred nanometers of the tip. Experiments with a diverging beam from an optical laser show that this arrangement produces clear images of objects sitting on a mirror. As expected, the objects are surrounded by Fresnel fringes (corresponding to the defocus distance from the tip to the mirror). As in the transmission case, these images can also be interpreted as in-line electron holograms, and so reconstructed to remove the Fresnel fringes. If the viewing screen lies parallel to the mirror as shown, the magnification is constant across the field of view and there is no foreshortening.

Our experimental PRM instrument is shown in figure 5 . Note that the image is not formed by scanning the tip, which remains stationary. Here A is the Burleigh inchworm used for tip approach (range lcm, smallest increment 4 nm). The tip is mounted in a hemisphere supported by three tangential pads whose normals are orthogonal and radial to the hemisphere. Two of these (E) are shear-mode piezos which rotate the hemisphere B about two axes (normal to the pads) by the "stick-slip" mechanism. The tip is positioned at the center of the sphere, so that eucentric tip rotation is obtained without translation. By controlling the ramp voltages supplied to the piezos the direction of the beam may thus be controlled. The third symmetrically disposed electrode supplies voltage to the hemisphere and tip, which is maintained during rotation. The GaAs sample is advanced laterally into the divergent beam by a second inchworm. The direct (D) and reflected (S) beams are indicated. A pumped load-lock at G allows either the sample to be removed, or, subsequently, after extending the vertical inchworm upward, the hemisphere containing the tip may be exchanged. The samples are cleaved in the load-lock. An internal mu-metal cylinder surrounds the instrument to reduce time dependent magnetic fields. The microscope sits on a 60 L/S ion pump, whose magnets generate magnetic fields which cancel along the optic axis. The entrance face of the channel plate may be biased negative to provide simple high pass energy filtering - this is found to improve the contrast of the images. However a bias voltage within less than about 50 volts of the beam voltage extinguishes the image entirely, indicating both the decline in efficiency of the MCP at low energies and the fact that many electrons are scattered inelastically[12]. Under typical operating conditions (depending on tip sharpness) a tip voltage of –350 V and an MCP bias of –300 volts were used. A multi-electrode LEED mesh optics system is planned for the future.

The patterns produced by this instrument may be understood using a combination of classical ray-tracing techniques and multiple scattering RHEED computations. The aberrations of the virtual source inside a nanotip field-emitter have been fully investigated in previous work[21], and the high brightness of these emitters measured[19]. The ray-tracing calculations are useful for predicting the image distortions for this optical system, which does not have circular symmetry. We have calculated the electron ray paths using the Munro ray-tracing programs, which solve La Place's equation for the boundary conditions defined by the electrodes and potentials and then obtain the

static electric field distribution. The motion of electrons launched from the tip is then solved for under the action of the Lorentz force. A mesh of variable spacing is used, with very fine sampling near the tip. No symmetry is assumed. The results are shown in figure 6, where the tip S , the grounded mirror, equipotentials, emitted and specular rays are all shown. Lines following around the tip are equipotentials, radial lines are electron trajectories. The field near a spherical tip of radius r on a shank at potential V is $E \approx V/kr$, with shape factor $k \approx 5$, independent of z_1 to a good approximation if $z_1 >> r$. We use tip asperities with $r < 10$ nm. The incident angles at the sample vary from –2 to 18 degrees. The failure of virtual rays to meet when projected back to a point near S' defines the image aberrations. The experimental full emission angle is about 14 degrees[21]. These computations show the closest approach possible without severe image distortion - the aberrations at S' may be measured as a function of the tip-sample distance z_1. We note that electrons do not travel from the tip in the direction normal to the sample surface by the shortest path. Rather, the trajectory is dominated by the orientation of local asperities on the tip, in the neighborhood of which the potential falls off rapidly and elections gain most of their kinetic energy. Thus the direction of the beam can be controlled by the tip goniometer if $z_1 >> r$. The calculations also show that the cross section of the beam changes from a circle to an thin ellipse, whose long axis lies in the plane of the surface, as the beam approaches the sample. Thus, while the range of azimuth angles is unchanged, the range of altitude angles in the incident cone decreases as electrons approach the surface, where they become a fan, or line source at the surface.

Diffraction effects are also seen in the patterns, including Bragg lines and Fresnel fringes at surface steps, as in LEEM imaging. Figure 7 shows the Bragg lines obtained when the tip is close to the sample. These lines are the locus of the RHEED Bragg condition for the incident ellipse of electrons. The angular compression of altitude angle by the electric field between sample and tip produces lines rather than disks, and the patterns can be indexed accordingly. Figure 8 shows a geometric simulation based on Bragg's law and the RHEED construction for the locus of these lines, in agreement with our observations, assuming a fan of incident rays covering a range of azimuth angles but a single altitude angle. Multiple electron scattering calculations are needed to account for these rocking curve intensities[15, 23-29]. A full

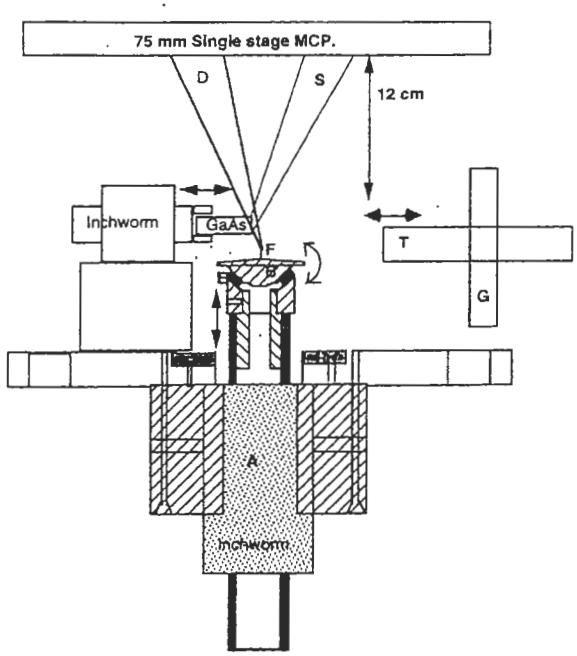

Fig. 5 The low voltage point reflection electron microscope. F-field emission tip. D,S-Direct and Specular reflected cone of rays. A-Inchworm for vertical tip motion. E-Shear mode piezos for tip rotation using hemisphere B. T-transfer device to replace tip or sample through loadlock G.

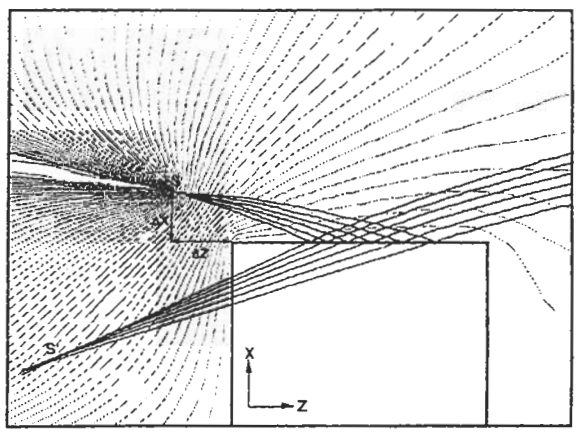

Fig. 6 Electron trajectories near tip (at –450 volts) and potentials, divided into 50 equipotentials. The width of the sample is 0.5mm along z.Δx=0.15mm. Crossover of rearward-projected beams defines virtual source S'below the surface. Rays propagating to the right produce a shadow image, or in-line hologram, of steps on the surface. Only the specular beam ((000) RHEED beam) is shown.

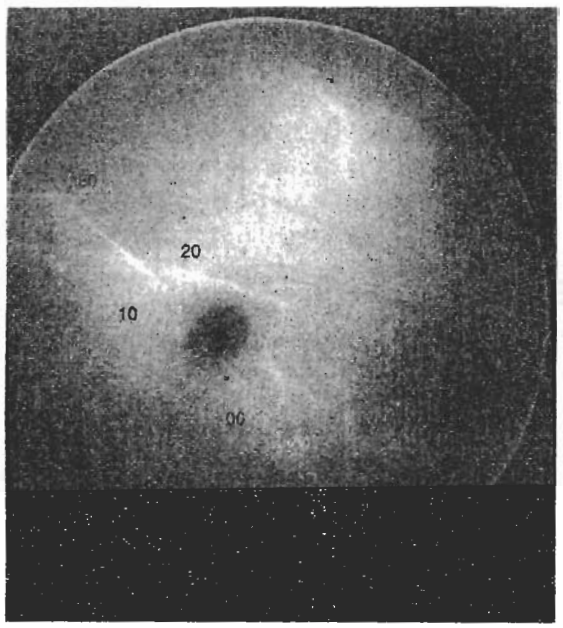

Fig. 7 Reflection diffraction pattern observed at −450V. Pattern is almost symmetric. Lines are indexed by their associated RHEED surface rod. The surface normal lies in the plane of the page at 45° to the horizontal. The beam is into the page.

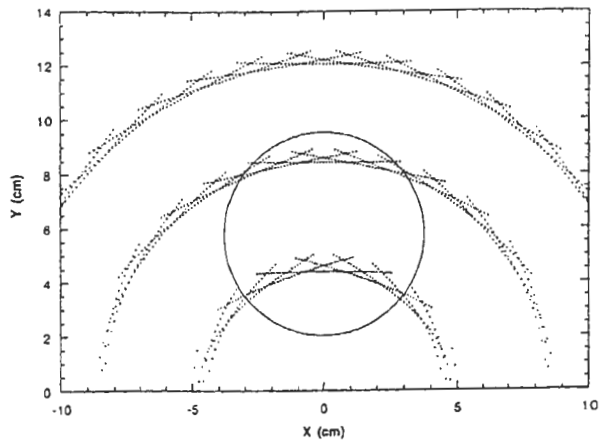

Fig. 8 Simulated lines pattern from three (+1, 0, −1) Laue zones (from bottom to top). GaAs (001) surface without reconstruction. Electron voltage −450 volts. The incident beams lies within a sheet. Altitude angle 32 degrees, azimuth angles −12 to 12 degrees around (100). The diameter of the circle is 75mm, the same as that of the MCP. Sample to screen distance 145mm. The bottom line of the figure (y=0) corresponds to the horizon or shadow edge of the sample surface.

treatment must also consider effects such as combined elastic and inelastic scattering along lines where Bragg, channeling or resonance conditions are fulfilled. At high energies these have been classified as "surface parabolas" (where a specular spot coincides with a horizontal Kikuchi line[30], Circles (due to elastic channeling along atomic strings[31], and two-dimensional Channeling Parabolae[32]. We have described a Bloch-wave perturbation method for calculating a shadow image (or in-line reflection hologram) from a surface step, including all multiple scattering effects in the bulk[15]. These diffraction results will be important when higher resolution images can be obtained.

If the tip is moved along the z axis in figure 6 away from the sample, the elliptical distortion is reduced, and the Bragg lines broaden into disks with diffuse edges. Images such as that shown in figure 9 are then observed. The diverging beam from the tip generates a complete rocking curve on the detector screen simultaneously in every order. (Each arrow in figure 9 lies in a different diffracted order). These rocking curves also contain shadow images of the crystal surface, exactly as in photoemission holography, in-line electron holography, or out-of-focus transmission convergent beam electron diffraction (CBED). Figure 9 was recorded using a liquid nitrogen cooled CCD camera, lens-coupled to the single-stage channel plate, with an exposure time of 0.2 seconds. A high pass filter was also used. The black spot is probably due to ions impinging on the nanotip, reducing emission locally. A point projection image of the tip is superimposed on the pattern, as in the field emission electron microscope, causing a slowly varying background. Close examination reveals that this image actually consists of four images of the same region of the surface, each projected from a slightly different point. Identical features can be recognized in each of the four bright patches, which lie approximately at the corners of a square. We thus assume that figure 9 shows four "convergent beam" disks (Bragg orders), each containing a shadow image of the heavily stepped cleavage surface. The centers of the bright image patches give the intersection of the Ewald sphere with the reciprocal lattice rods, whose orientation is known and approximately vertical in figure 9. The crystal surface runs across the bottom of the picture. This suggests that the lower images are formed in ZOLZ rods while the upper pair may be first order Laue Zone rods. For this image, the tip-to-sample distance z_1 was about 0.5mm, giving a magnification of about 200. At this low magnification, Fresnel edge fringes

from surface steps are not expected. To confirm this interpretation, optical microscope images of the same region were obtained from the sample after removal from the chamber.

Figures 10 shows the geometry we have used to interpret these results. In figure 10, one virtual source s' exists inside the sample for each Bragg beam and reciprocal lattice rod. Each source projects a different view of the same region of surface illuminated by the beam. As indicated , it seems likely that our shadow images of the surface are formed from the specular, ZOLZ and FOLZ rods.

The ray-tracing calculations show that images should be obtainable at higher magnification, limited only by the mechanical precision of the stick slip manipulators. The ray tracing calculations show that at small values of the tip-sample gap z_1 , the elliptical distortion of the beam is again reduced, and full-field imaging should again be possible. Eventually, at very small (nanometer) values of z_1, calculations show that electrons emitted from the tip cannot escape from the tip field, and bounce along the surface until absorbed in the sample. Calculations are under way to evaluate all these effects further. At high resolution,

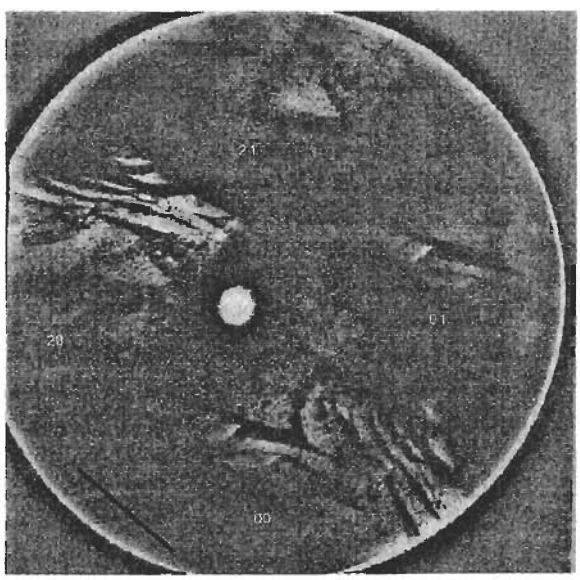

Fig. 9 Reflection shadow images of cleaved GaAs surface, obtained at 450volts. Magnification about 200. This picture consists of four different images of the same surface features recorded in four different Bragg beams. Each shows the heavily stepped cleavage suface. The sample surface runs across the bottom of the figure. (In figure 10 the lower two bright regions above are labeled St, the upper ones Wk).

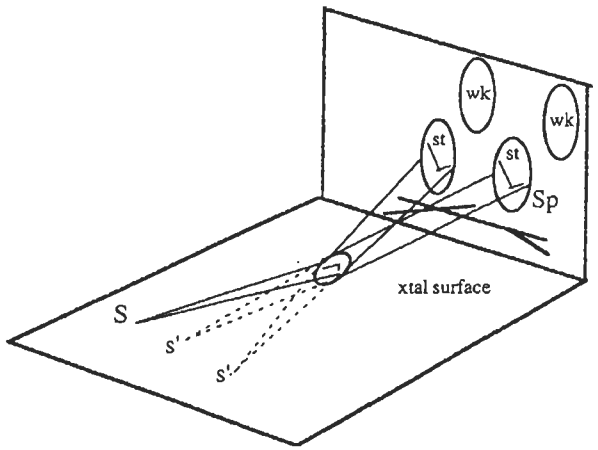

Fig. 10 Simplified geometry of shadow image formation in several beams simultaceously from virtual sources s'inside the crystal, below the surface. The diffraction orders strong (St) and weaker HOLZ reflections (wk) correspond to the four bright areas in figre 9. The specular beam Sp is indicated.

Fresnel edge fringes should be seen at surface steps, and these might be removed by holographic image processing, as has already been done for images recorded in the transmission point-projection geometry[33].

We note that atomic resolution Fourier lattice images will be observed in the region where adjacent coherent orders overlap and interfere[34]. For the Si 7×7 (111) surface, which involves much smaller diffraction angles, these results show that adequate angular coherence exists.

An important improvement in image quality will be obtained with the provision of multi-electrode LEED screens for energy filtering, since the present arrangement results in electrons entering the MCP with less than 50 eV energy. At this energy the MCP efficiency is very low. The use of a re-acceleration screen will improve the images considerably. Alternatively, an imaging Wein filter might be considered[35]. Since the region illuminated under the tip may be as small as a few nanometers, the instrument might also provide a useful form of microdiffraction from bulk samples, in conjunction with imaging. The use of an electrostatic gun lens to form a cross-over before the sample would limit the resolution to that of the electrostatic lens, reduce brightness and introduce formidable alignment problems in the gun electrodes. We note that the instrument provides several simultaneous stereographic projections of the same surface feature, so that three-dimensional re-

construction (holographic or otherwise) should be possible. Simulations have also been completed for the PRM image of a superconducting vortex emerging at a surface - these show good phase contrast, suggesting that the instrument might be useful for the study of vortex dynamics, where high resolution is not required but good phase contrast is required.

In summary, if higher quality images can be obtained at higher magnification, the advantages of this instrument include low cost, small size, high image recording speed (for dynamic experiments), three-dimensional imaging, and lack of complexity. The lensless design almost eliminates spherical aberration, however the aberrations of the virtual source must be considered[21]. Disadvantages include the image distortions which may limit performance at moderate magnification. These have yet to be investigated in detail.

Acknowledgments

This work was supported by NSF award DMR9526100. Experimental work on the STAP project was performed by U. Weierstall, and by X. Zhang on the PRM project. I am particularly grateful to Profs G. Smith and D. Seidman for their interest and encouragement on the STAP project.

References

1. P. Avouris Ed., *Atomic scale modlfications of material*. Nato ASI Series Vol **E239**. (Plenum, New York, 1992). See also J.Wiesendanger, Scanning Probe Microscopy and Spectroscopy (C.U.P., Cambridge, UK., 1994) and *J. Vac Sci.* **B12 (3)** (1994)
2. C.J. Chen, Scanning Microscopy, Supplement 7, p.281 (1993)
3. J.C.H.Spence and U. Weierstall. J. Vac. Sci. Technol. B14, p.1587 (1996)
4. P. E. Batson, *Nature* **366**, 727 (1993).
5. G. Hembree, J. Drucker, F. Luo, M. Krishnamurty, J. Venables, *Appl. Phys. Lets.* **58**, I (1991)
6. M. Miller and G. Smith, *Atom Probe Microanalysis* (Materials Research Society, Pittsburgh 1989)
7. T. Sakurai. *Prog. Surf Sci.* **33**, I (1990); O. Nishikawa et al.*J.Vac.Sci.Tech.* **B13** 599 (1995)
8. W. Lo and J.C.H. Spence, *Ultramic.* **48**, 433 (1993),
9. J.A. Panitz, *Rev. Sci. Instr.* **44** 1034 (1973).
10. R. Becker, J. Golovchenko, B. Schwartzentruber. *Nature* **325** 419 (1987).
11. P. Avouris and L. Lyo. *Applied Surface Science* **60** 426 (1992); W.Mizutani et al *Appl. Surf. Sci.* 87/88 399 (1995)
12. K. Kobayashi et al. in ref 1. (Avouris, Ed.).
13. L. Whitman, J. Strocio, R. Dragoset, R. Celotta p 25. in ref I ., Avouris Ed.
14. G. Kellogg, *Prog. Surf. Sci.* **21** 1 (1994).
15. J. Spence, X. Zhang, U.Weierstall and J. Zuo. Surface Review and Letters (1997) in press.
16. G. A. Morton and E. G. Ramberg, Phys. Rev., 56,705 (1939)
17. V.Binh, Ultramic, 58, 307 (1995); Also J. Spence, W. Qian, X. Zhang Ultramic 55,19 (1994)
18. H. W. Fink, H. Schmid, H. J. Kreuzer and A. Wierzbicki,Phys. Rev. Letts., 67,1543 (1991)
19. J. Spence, W. Qian and M. Silverman, J. Vac. Sci. Tech., A12, 542 (1994)
20. N. Yao and J. M. Cowley, Ultramic., 31,149 (1989)
21. M. Scheinfein, W. Qian and J. C. H. Spence, J. Appl. Phys., 73, 2057 (1993)
22. L. Reimer,Scanning electron microscopy (Springer,Berlin, 1985)
23. T. Kawamura, T.Ichinokawa, Y.Watanabe and H.Wada, Inst. Phys. Conf. Ser, 41,223 (1978)
24. A. Gervais, R. Stern and M. Menes, Acta Cryst., A24, 191 (1968)
25. J. M. Cowley and L. Peng, Ultramic., 59, 59 (1985)
26. L. M. Peng, S. L. Dudarev and M. J. Whelan, Acta Cryst. A52, 909 (1996)
27. L. M. Peng and M. J. Whelan, Proc. Roy. Soc. Lond., 43 1,125 (1990)
28. T. Zhao, H. Poon and S. Tong, Phys. Rev., B38,1 172 (1988)
29. A. Ichimiya, Jap. J. Appl. Phys., 22,173 (1983)
30. A. Ichimiya, K. Kambe and G. Lehmpfuhl, J. Phys. Soc. Jpn., 49,684 (1980)
31. G. Lehmfuhl and W. Dowell, Acta Cryst, A42,569 (1986)
32. L. Wang and J. Cowley, Ultramic., 55, 228 (1994)
33. J.Spence, X.Zhang, W.Qian, in "Electron Holography". Ed.A.Tonomura, Elsevier, (1995), 267
34. J. C. H. Spence and J. M. Zuo, Electron

Microdiffraction (Plenum, New York,1992)

35. H. Rose, Optik, 77, 26 (1987). See also K. Tsuno, Rev. Sci. Instr., 64, 659 (1992)